View metadata, citation and similar papers at core.ac.uk
brought to you by CORE
provided by HZB Repository

JOURNAL OF APPLIED PHYSICS 99, 123511 (2006)

Ion-beam induced effects at 15 K in α-Al_2O_3 of different orientations

C. S. Schnohr, E. Wendler,[a] K. Gärtner, and W. Wesch
Institut für Festkörperphysik, Friedrich-Schiller-Universität Jena, Max-Wien-Platz 1, D-07743 Jena, Germany

K. Ellmer
Hahn-Meitner-Institut Berlin, Glienicker Strasse 100, D-14109 Berlin, Germany

(Received 7 February 2006; accepted 14 April 2006; published online 23 June 2006)

Ion-beam induced effects in α-Al_2O_3 of *c*, *a*, and *r* orientations were studied by Rutherford backscattering spectrometry (RBS) in channeling configuration using 1.4 MeV He ions. 150 keV Ar, 150 keV K, or 80 keV Na ions were step by step implanted at 15 K followed immediately by the RBS analysis without changing the sample environment. Defect annealing was observed during the RBS measurement, which is attributed to the electronic energy loss of the He ions. A similar effect occurs due to the electronic energy loss of the implanted ions, resulting in a reduced defect concentration between surface and profile maximum. The electronic energy loss of ions may change the charge state of defects, thus enhancing their mobility and causing defect annealing. The results suggest that within the collision cascade of individual ions in perfect sapphire only point defects are produced, the concentration of which is well reproduced by SRIM calculations taking into account suggested values of the displacement energies of $E_d^{Al}=20$ eV and $E_d^{O}=50$ eV for aluminum and oxygen, respectively. The lower efficiency for point defect production measured in *c*-oriented material can be explained by the heavily reduced visibility of Al atoms sitting on vacant octahedral sites, which are hidden in this direction. Point defect recombination is observed when the collision cascades start to overlap. Above a critical concentration point defects are altered into clusters which rapidly grow during further irradiation until a saturation is reached. © *2006 American Institute of Physics*. [DOI: 10.1063/1.2204748]

I. INTRODUCTION

Ion irradiation in sapphire has been much studied during the last three decades because of its many technical applications (see reviews in Refs. 1–4 and references therein). Much work has been done on damage formation, amorphization, and annealing behavior of implanted sapphire under various conditions for a great number of implanted ion species.

It was found that implantation at room temperature leads to a complex defect structure and needs anomalously high ion fluences in the order of 10^{16}–10^{17} cm^{-2} to render the material amorphous.[5,6] Furthermore, the chemical nature of the implanted species plays a prominent role in the amorphization behavior at this temperature.[7,8] At temperatures well below room temperature it is assumed that implantation produces the amorphous state by damage accumulation alone at ion fluences relatively low in comparison to those necessary for amorphization at room temperature.[2,9]

Differences in the damage-accumulation behavior for samples of different crystal orientation have been reported.[10–12] For implantation in *c*-oriented samples, smaller ion fluences are needed to reach maximum damage than for *a*-oriented samples. However, no systematic study and comparison of the damage evolution for samples of different crystal orientations have been reported so far.

This work presents the results of the investigations of damage formation in α-Al_2O_3 of three different orientations under irradiation with three different ion species implanted and measured at 15 K. Because at this low temperature thermal effects are widely excluded, the lattice damage observed by Rutherford backscattering spectrometry (RBS) in channeling configuration is mainly ion-beam induced. The application of a sophisticated software enables us to determine the depth distributions of the damage produced by the implanted ions. Different from most of the studies mentioned above, which focus on the implantation of higher ion fluences, the present paper concentrates on the primary effects of damage production and accumulation, starting at very low ion fluences.

II. EXPERIMENTAL DETAILS

In the present studies we used high-quality single crystals of α-Al_2O_3 obtained from Crystec with *c*, *a*, and *r* orientations. These are defined by a (0001), a $(11\bar{2}0)$, and a $(01\bar{1}2)$ surface plane, respectively. All experiments presented here were conducted in a double beam target chamber.[13] This allows us to perform a series of subsequent ion implantations each followed immediately by the RBS measurement without changing the sample environment. The target holder was cooled down to a temperature of 15 K using a cryogenic system. The samples were fixed on the target holder with conductive silver lacquer in order to realize sufficient heat and charge transfer.

For implantation three different ion species were chosen, namely, 80 keV Na and 150 keV Ar for all orientations as well as 150 keV K for the *c*-oriented samples (for details see

[a]Electronic mail: wendler@pinet.uni-jena.de

 © 2006 American Institute of Physics

Downloaded 31 Aug 2007 to 134.30.24.17. Redistribution subject to AIP license or copyright, see http://jap.aip.org/jap/copyright.jsp

TABLE I. Data for the different series of implantations ($S0$, $S1$, $S2$, and P) performed with Ar, K, and Na ions into α-Al_2O_3 of c, a, and r orientations. A series of implantation starts with a fluence N_I^{first} and then the fluence is enhanced step by step, each followed immediately by the RBS measurement. The final fluence reached is N_I^{total}. The series P is especially used to investigate the He beam induced annealing in more detail (see Sec. III B). N^*_{displ} stands for the maximum value of the Al displacements per ion and unit depth as calculated by SRIM2003.

Energy (keV)	ion	N^*_{displ} (10^7 cm^{-1})	Sample type	series	N_I^{first} (10^{14} cm^{-2})	N_I^{total} (10^{14} cm^{-2})	number of steps
150	Ar	8.30	c	$S1$	0.6	8.0	6
				$S2$	4.0	40	6
				P	5.4	10	2
			a	$S1$	0.4	28	12
				$S2$	10	90	7
				P	5.4	10	2
			r	$S0$	0.2	0.7	3
				$S1$	0.5	20	11
				$S2$	4.7	40	7
				P	4.0	6.0	2
150	K	8.65	c	$S1$	0.5	14	8
				$S2$	11	35	5
80	Na	4.64	c	$S1$	1.0	40	10
			a	$S1$	1.0	20	7
				$S2$	20	130	6
			r	$S1$	0.4	50	10

Table I). Implantation took place 7° off axis in order to avoid channeling effects for the implanted ions. The current density was kept between 0.1 and 0.5 μA cm^{-2}.

The analysis was done with RBS channeling measurements along the crystal axis normal to the surface (corresponding to the sample orientation) using 1.4 MeV He ions and a backscattering angle of $\vartheta=170°$. The beam current did not exceed the value of 10 nA while the spot size diameter was 1 mm. The yields of the aligned spectra for the perfect (unimplanted) and the damaged crystal, $Y_{\mathrm{al}}^{\mathrm{perf}}$ and $Y_{\mathrm{al}}^{\mathrm{dam}}$, respectively, as well as the yield of measurement in random direction, Y_{ra}, were used to calculate the minimum yields of the perfect crystal, $\chi_{\mathrm{min}}^{\mathrm{perf}}=Y_{\mathrm{al}}^{\mathrm{perf}}/Y_{\mathrm{ra}}$ and the damaged crystal $\chi_{\mathrm{min}}^{\mathrm{dam}}=Y_{\mathrm{al}}^{\mathrm{dam}}/Y_{\mathrm{ra}}$. The difference in minimum yield, $\Delta\chi_{\mathrm{min}}=\chi_{\mathrm{min}}^{\mathrm{dam}}-\chi_{\mathrm{min}}^{\mathrm{perf}}$, was taken as a measure for the amount of damage produced.

Depth profiles of damage were calculated from the Al part of the measured minimum yield using the latest version of the computer code DICADA.[14] This program describes axial dechanneling in compound crystals with point defects based on a modified master equation. Due to the complex structure of sapphire a new feature was included. Strings of atoms (in the channeling direction) with very small distances (<0.4 Å) are summarized to one so-called *averaged* string which is not a perfect string but contains displaced atoms. Using DICADA with this modification the relative concentration of displaced lattice atoms, n_{def}, versus depth z was obtained for each crystal orientation. In the following text n_{def} is referred to as defect concentration.

For comparison, the depth distributions of primary displacements were calculated with the computer code SRIM2003 (Ref. 15) for the three different ion species implanted. The displacement energies were set to $E_d^{\mathrm{Al}}=20$ eV and $E_d^{\mathrm{O}}=50$ eV for aluminum and oxygen, respectively.[3] The resulting maximum number of Al displacements per ion and unit depth, N^*_{displ} (see Table I), was used to convert the ion fluence N_I to displacements per atom by $n_{\mathrm{dpa}}=(N_I N^*_{\mathrm{displ}})/N_0$ where N_0 denotes the Al particle density ($N_0=4.712\times10^{22}$ cm^{-3}).

III. EXPERIMENTAL RESULTS

A. Depth distribution of defects

As an example for the damage evolution measured as a function of the ion fluence, Fig. 1 shows the energy spectra of backscattered He ions measured in channeling configuration for implantation of 80 keV Na into c-, a-, and r-oriented samples. With increasing ion fluence a buried damaged layer is produced, the peak of which reaches the random level at $N_I\approx2.5\times10^{15}$ cm^{-2}, $N_I\approx6.0\times10^{15}$ cm^{-2}, and $N_I\approx3.0\times10^{15}$ cm^{-2} for c, a, and r orientations, respectively. Further implantation leads to the expansion of the damaged region until, finally, the aligned yield shows random level up to the surface.

The defect profiles were calculated from the Al part of the minimum yield $\chi_{\mathrm{min}}^{\mathrm{dam}}$ as described in Sec. II assuming the atoms to be randomly displaced from their lattice sites. Figure 2 shows the profiles for c-, a-, and r-oriented samples implanted with 150 keV Ar ions up to four different ion fluences.

For the two lowest ion fluences (see Fig. 2) the experimental defect distributions are slightly narrower than the SRIM ones with similar widths for all orientations. Furthermore there is a pronounced dip in the profiles between the surface and the buried damaged layer, which the SRIM calculations do not exhibit. A comparison of the profiles of the two higher ion fluences shows differences in the shape of the defect distributions for the different crystal orientations. The c-sample profiles stay narrow and unshifted until the random level is reached and only then do they start to grow towards the surface and into greater depth. For the a and the r sample the peak broadens already before the random level is reached. This starts at a critical maximum defect concentration of $n_{\mathrm{def}}^a(\max)\approx0.6$ and $n_{\mathrm{def}}^r(\max)\approx0.8$ for a and r orientations, respectively.

A comparison of the profiles for the different ion species yields the result that in all cases the depth of the maximum is only marginally deviating from the SRIM prediction.[16,17] In relation to the calculated profiles, the defect distributions measured for Ar or K implantation are slightly shifted to larger depths than the ones for Na implantation. Apart from that, there is no significant effect of the ion species observable for all orientations.

During the RBS measurement we observed a defect annealing (see Sec. III B). However, by comparing the profiles for a given ion fluence resulting from two subsequent RBS measurements, it was proved that this annealing does not alter the shape of the distribution and thus does not account for the dip in the measured profiles. However, its influence on the absolute value of defect concentration cannot be neglected as will be discussed in the following.

Downloaded 31 Aug 2007 to 134.30.24.17. Redistribution subject to AIP license or copyright, see http://jap.aip.org/jap/copyright.jsp

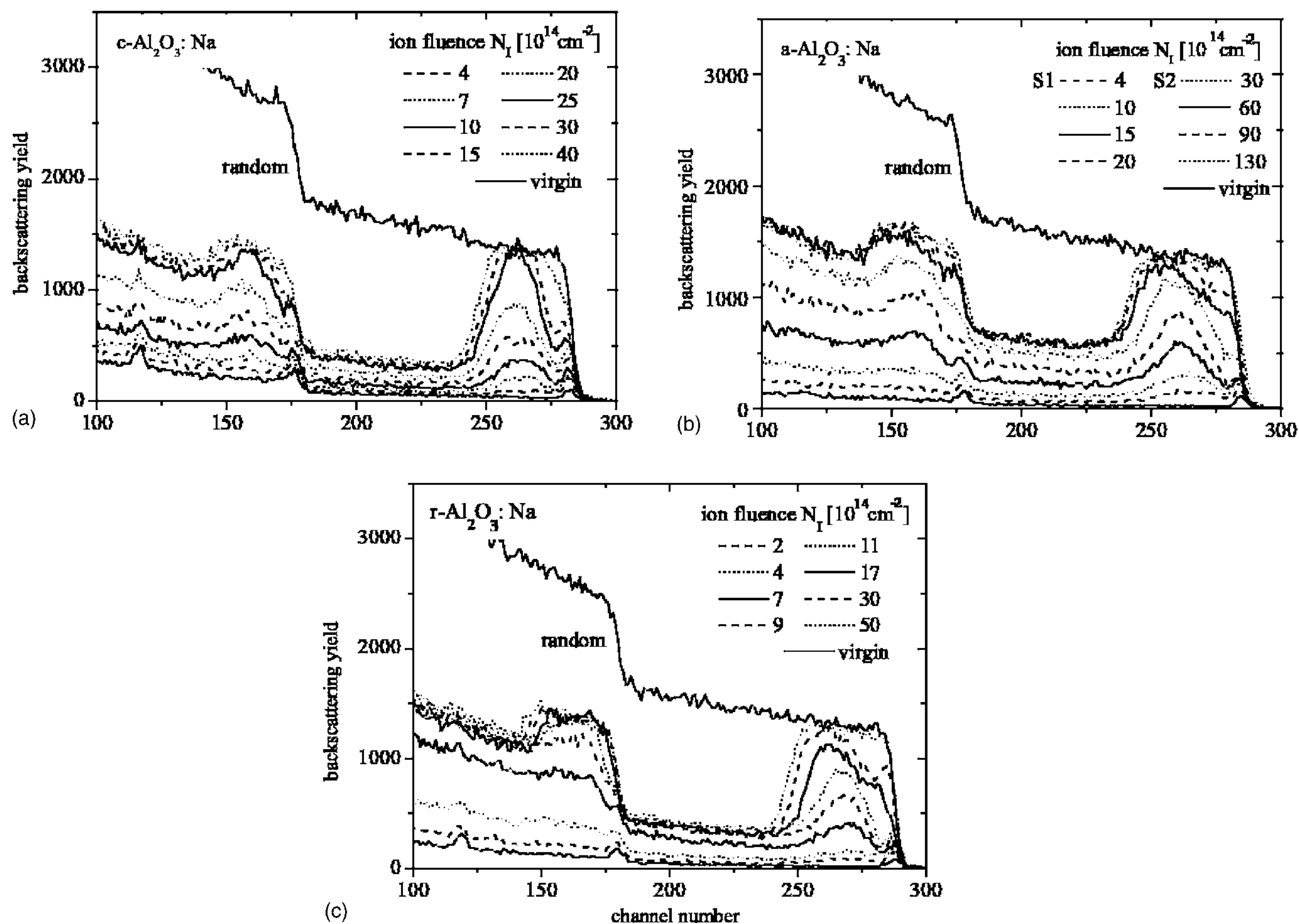

FIG. 1. RBS channeling spectra of 1.4 MeV He ions backscattered on c-Al_2O_3 (a), a-Al_2O_3 (b), and r-Al_2O_3 (c) implanted with 80 keV Na at 15 K (no change of temperature between implantation and measurement). $S1$ and $S2$ in (b) denote series measured on different samples.

B. He beam induced annealing

In order to study the effect of the He irradiation during the RBS measurement on the defect concentration, each RBS measurement was performed in steps of equal charges, providing a series of spectra (called subspectra). Additionally, in some cases prolonged measurements using up to three times the total He charge of a normal spectrum were performed with the same measured He charge for all these *subspectra*. Figure 3 shows an example of such a prolonged measurement for each crystal orientation. For better statistics, the difference in minimum yield, $\Delta\chi_{\min}^{\text{subspectra}}(\text{int})$, was calculated after integrating the yields within the depth range of damage. The results clearly show a decrease in the backscattered yield of the Al peak with increasing number of subspectra, which is proportional to the He charge. As can be seen from Fig. 3 the annealing effect is smallest for c orientation and largest for r orientation.

Since we did subsequently several implantation and RBS measurement steps on the same sample, this annealing effect leads to the situation that the fluence dependence of damage caused by implantation without any RBS measurement (undisturbed damage accumulation) cannot be obtained directly from the experimental data as is illustrated in Fig. 4. Although the annealing for each data point itself is small, the effect adds up, resulting in a significant deviation of the measured data from the curve one would observe without annealing during the measurement.

In order to obtain the undisturbed fluence dependence, a special simulation procedure has been developed. The main idea is to describe the undisturbed fluence dependence of $\Delta\chi_{\min}$ by an analytical formula with a set of free parameters. Further, the effect of the annealing during the RBS measurement is parametrized by a careful analysis of $\Delta\chi_{\min}^{\text{subspectra}}$ versus the number of subspectra, i.e., versus the He charge (for details see Ref. 17). Then the formula of the damage-accumulation model is used to simulate the defect concentration, which is to be expected for a given ion fluence, but without influence of the measurement. In a second step the resulting defect concentration is reduced according to the He beam induced annealing during the measurement. This reduced defect concentration is then the starting value to simulate the effect of the next implantation step with the damage-accumulation model (see Fig. 4). The parameters of the analytical model have to be chosen in such a way that the calculated reduced defect concentrations do agree with the experimental values. By this fitting procedure the free parameters are obtained and the undisturbed curves of damage accumulation can be calculated using the model without the intermediate annealing steps due to the measurement (see

Downloaded 31 Aug 2007 to 134.30.24.17. Redistribution subject to AIP license or copyright, see http://jap.aip.org/jap/copyright.jsp

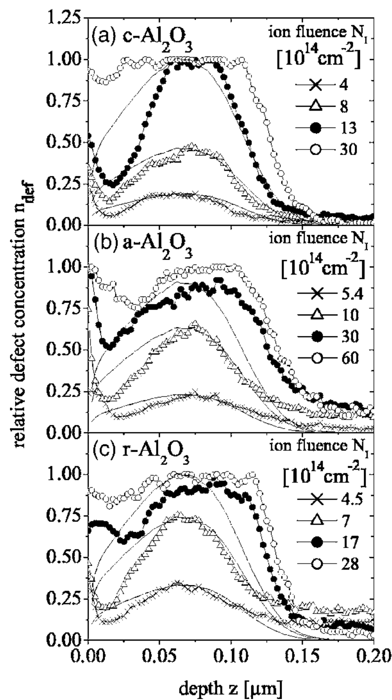

FIG. 2. Relative concentration of displaced lattice atoms, n_{def}, vs depth z calculated from the Al part of the RBS spectra for implantation of c-oriented (a), a-oriented (b), and r-oriented (c) Al_2O_3 with 150 keV Ar at 15 K. The distributions of primary displaced atoms calculated by SRIM2003 are added in arbitrary units, each chosen to fit the corresponding maximum value (solid lines).

Fig. 4). In the next section it is shown how the damage-accumulation model is deduced from the analysis of the experimental data and an example for the fitting procedure described above is given.

C. Fluence dependence of damage accumulation

1. Experimental results $\Delta\chi_{min}^{exp}$ versus n_{dpa}

For the analysis of the damage-accumulation process the difference in minimum yield at the maximum of the distribution, $\Delta\chi_{\mathrm{min}}^{\mathrm{exp}}$, was taken as a measure of the amount of damage produced during the implantation, because for all cases investigated here the relative defect concentration n_{def}

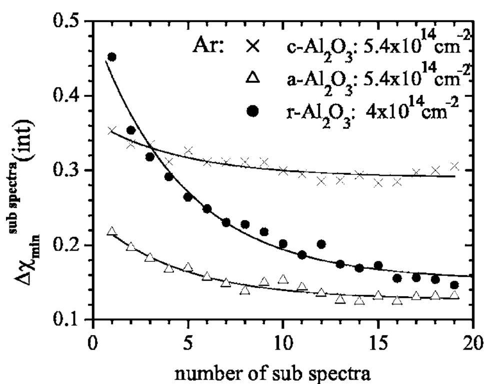

FIG. 3. Difference in minimum yield $\Delta\chi_{\mathrm{min}}^{\mathrm{subspectra}}(\mathrm{int})$ calculated after integrating the yields within the depth range of damage in the RBS channeling subspectra after implantation of Ar into c-, a-, and r-oriented Al_2O_3 at 15 K vs the number of measured subspectra. The solid lines show the best exponential fit.

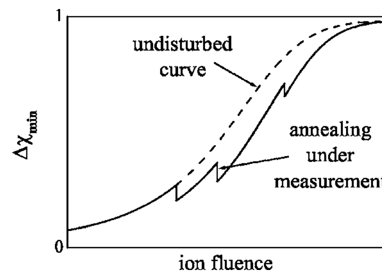

FIG. 4. Illustration of the consequence of He irradiation induced annealing during the RBS measurement on the damage accumulation represented by $\Delta\chi_{\mathrm{min}}$ vs ion fluence (solid line: fitted fluence dependence taking annealing into account; dashed line: undisturbed curve to be expected from the same fluence dependence but without annealing).

is equal to $\Delta\chi_{\mathrm{min}}^{\mathrm{exp}}$,[17] and the He beam induced annealing was analyzed for $\Delta\chi_{\mathrm{min}}$. Figure 5 shows the experimental values, $\Delta\chi_{\mathrm{min}}^{\mathrm{exp}}$, determined from the RBS spectra measured with full He charge as a function of ion fluence. For comparison of the results for the various ion species the latter has been converted to n_{dpa} (see Sec. II). Already from these (uncorrected) experimental data it can be seen that for all orientations the results for the different ion species show a uniform dependence on the displacements per atom (dpa). No significant *chemical* effect of the implanted ions is observable.

In the double-logarithmic plot for the c-oriented samples [Fig. 5(a)] mainly two regions of damage production can be distinguished. For low n_{dpa} values up to 0.4, $\Delta\chi_{\mathrm{min}}^{\mathrm{exp}}$ increases almost linearly with the ion fluence up to a value of about 0.03. For ion fluences above 0.4 dpa, a steeper slope of $\Delta\chi_{\mathrm{min}}^{\mathrm{exp}}$ is found which continues unchanged until the damage level ranges between 0.95 and unity, indicating that the peak maximum has reached the random level. This sharp edge can be seen more clearly in the half-logarithmic plot [Fig. 5(b)].

For the a- and r-oriented samples [Figs. 5(c) and 5(e)] three regions of damage accumulation can be seen. In the low n_{dpa} region up to 0.5 and 0.4 for the a and r samples, respectively, the data points show a weak increase (lower than linear) with ion fluence. At critical values of $\Delta\chi_{\mathrm{min}}^{\mathrm{exp}} \approx 0.10$ and $\Delta\chi_{\mathrm{min}}^{\mathrm{exp}} \approx 0.06$ for a and r orientations, respectively, the increase of the data points changes such that for ion fluences above 0.5 and 0.4 dpa, respectively, a steeper slope similar to that of the c samples is observed. However, a third region is formed where the increase of $\Delta\chi_{\mathrm{min}}^{\mathrm{exp}}$ lessens once more, slowing down the approach to unity and indicating another change in the damage-accumulation process. This leads to a rounded and flattened curve near the random level, which can be seen more clearly in the half-logarithmic plot [Figs. 5(d) and 5(f)]. This third region corresponds to the range of peak broadening observed in the defect distributions of a- and r-oriented samples discussed in Sec. III A (see Fig. 2).

Because of the low defect concentration of $n_{\mathrm{def}} \leqslant 0.1$ within the first region only isolated point defects are to be expected. The change in the accumulation rate within the second region is attributed to the occurrence of a second type of defects that is referred to as clusters. However, their true nature is not clear.

Downloaded 31 Aug 2007 to 134.30.24.17. Redistribution subject to AIP license or copyright, see http://jap.aip.org/jap/copyright.jsp

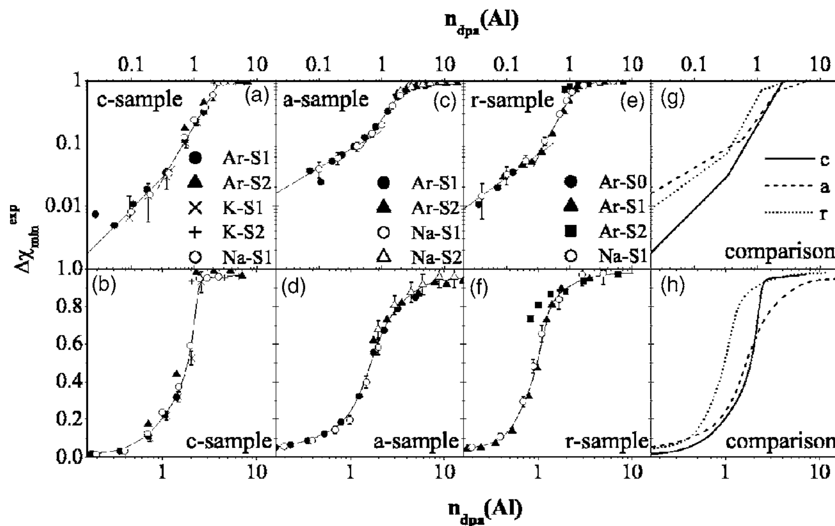

FIG. 5. Difference in minimum yield $\Delta\chi_{\min}^{\mathrm{exp}}$ calculated at the maximum of the Al peak after implantation of c-oriented [(a) and (b)], a-oriented [(c) and (d)], and r-oriented [(e) and (f)] samples vs displacements per atom, $n_{\mathrm{dpa}}(\mathrm{Al})$. For better visibility the data are given in double-logarithmic scale [(a), (c), and (e)] as well as in half-logarithmic scale [(b), (d), and (f)]. The solid lines are drawn to guide the eye. The experimental errors are shown for one data series only in order to avoid an overload of the graphs. *S*0, *S*1, and *S*2 denote measurement series on different samples. A comparison of the *eye guiding lines* is given in (g) and (h), again for double- and half-logarithmic plots, respectively.

2. Analytical model for the simulation

Starting from the discussion of the measured evolution of $\Delta\chi_{\min}^{\mathrm{exp}}$ with n_{dpa}, the following model (based on the model by Hecking *et al.*[18]) was developed:

$$\frac{dn_{\mathrm{pd}}}{dn_{\mathrm{dpa}}} = P_{\mathrm{pd}} \exp(-R_{\mathrm{pd}}^2 n_{\mathrm{dpa}}^2)(1-n_c) - F_c f(n_{\mathrm{pd}}) - G_c n_c \frac{n_{\mathrm{pd}}}{1-n_c}, \tag{1}$$

$$\frac{dn_c}{dn_{\mathrm{dpa}}} = [F_c f(n_{\mathrm{pd}}) + G_c n_c]\left(1 - \frac{n_c}{n_c^{\mathrm{sat}}}\right)^p, \tag{2}$$

$$\text{with} \quad f(n_{\mathrm{pd}}) = \left[1 - \exp\left(\frac{n_{\mathrm{pd}}^{\mathrm{crit}} - n_{\mathrm{pd}}}{0.001}\right)\right]^{-1}, \tag{3}$$

$$\text{and} \quad n_{\mathrm{pd}} + n_c = n_{\mathrm{def}} \approx \Delta\chi_{\min}. \tag{4}$$

It is assumed that two types of defects exist: point defects with the relative concentration n_{pd} and clusters with the relative concentration n_c, both contributing to the difference in minimum yield, $\Delta\chi_{\min}$, in the same way [see Eq. (4)]. With this the following model of damage accumulation is assumed. Within a single ion impact, only isolated point defects are produced with an efficiency denoted by P_{pd}. Recombination of point defects, occurring when the collision cascades start to overlap, is enabled with R_{pd} being the parameter for this process [see first term in Eq. (1)]. After a critical concentration of point defects, $n_{\mathrm{pd}}^{\mathrm{crit}}$, is exceeded, they are altered into clusters with a certain efficiency F_c [see second term in Eq. (1)]. The switching on of this process is described by the function $f(n_{\mathrm{pd}})$ [see Eq. (3)]. Further implantation leads to the stimulated growth of these clusters represented by the parameter G_c. The factor $(1-n_c/n_c^{\mathrm{sat}})$ secures that the relative concentration of these clusters does not exceed a certain saturation value, n_c^{sat}, in particular, that it does not exceed unity [see Eq. (2)]. The fact that $\Delta\chi_{\min}^{\mathrm{exp}}(n_{\mathrm{dpa}})$ for the *a* and *r* samples does not reach unity like a sharp edge as it was found for the *c* sample cannot be easily understood. Possibly a saturation of clusters occurs, which is superimposed by a beginning amorphization. However, our experimental data do not allow to distinguish between these processes. Therefore, the slow approach to unity in the cases of *a*- and *r*-oriented samples was modeled simply by using the factor $(1-n_c/n_c^{\mathrm{sat}})^p$ with $p>1$ that realizes the saturation of n_c without introducing a third type of defects [see Eq. (2)]. The way of doing so is not predicted by a physical process but it was the most reasonable approach to fit the measured data and finally to obtain the undisturbed damage-accumulation curves.

With the model presented, three regions of the dependence of $\Delta\chi_{\min}$ on n_{dpa} can be distinguished. Region I is given by $n_{\mathrm{pd}} < n_{\mathrm{pd}}^{\mathrm{crit}}$ and $n_c \approx 0$. This provides a linear dependence of $\Delta\chi_{\min}$ on n_{dpa} followed by a weaker dependence (like a plateau) in the case of a remarkable recombination. In region II beginning at $n_{\mathrm{pd}} \approx n_{\mathrm{pd}}^{\mathrm{crit}}$ the difference in minimum yield increases rapidly mainly by formation and growth of clusters. Region III is characterized by a continuous decrease of the slope of $\Delta\chi_{\min}$ until its saturation value of about unity is reached.

An example for a measured fluence dependence of $\Delta\chi_{\min}$ fitted with the help of Eqs. (1)–(4) and taking into account the He beam induced annealing as described in Sec. III B is shown in Fig. 6. It can be seen that the experimental results

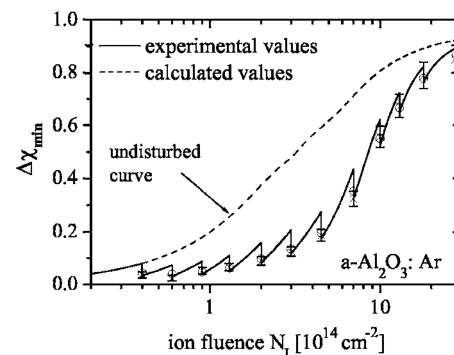

FIG. 6. Example of the fitting procedure for a series of data points measured after Ar implantation of a-Al_2O_3 at 15 K. The maximum values $\Delta\chi_{\min}$ are plotted vs the ion fluence N_I with the crosses denoting the experimental data points and the hollow circles being the calculated data points. The undisturbed fluence dependence thus obtained is shown as dashed line.

Downloaded 31 Aug 2007 to 134.30.24.17. Redistribution subject to AIP license or copyright, see http://jap.aip.org/jap/copyright.jsp

TABLE II. Values for the set of parameters of the analytical model [see Eqs. (1) and (2)] used in the simulation procedure as obtained from fitting the experimental data for the various implantation series.

Type	Ion	Series	P_{pd}	R_{pd}	n_{pd}^{crit}	F_c	G_c	n_c^{sat}	p
c	Ar	*S*1,*S*2	0.20	⋯	0.03	0.11	2.3	0.99	1.0
	K	*S*1,*S*2	0.15	⋯	0.03	0.11	2.8	0.97	1.0
	Na	*S*1	0.17	⋯	0.03	0.10	3.0	0.97	1.0
	Mean		0.17	⋯	0.03	0.11	2.7	0.98	1.0
a	Ar	*S*1	1.1	1.9	0.10	0.51	5.1	0.97	2.0
		*S*2	1.1	9.9	0.10	0.51	5.1	0.97	2.0
	Na	*S*1	0.76	2.0	0.10	0.56	5.3	0.98	2.0
		*S*2	0.76	6.5	0.10	0.56	5.3	0.98	2.0
	Mean	*S*2	0.97	8.3	0.10	0.54	5.2	0.98	2.0
r	Ar	*S*0	0.80	0.0	⋯	⋯	⋯	⋯	⋯
		*S*1	0.74	0.0	0.06	0.17	10	0.96	1.2
		*S*2	0.74	9.7	0.06	0.17	10	0.98	1.2
	Na	*S*1	0.81	2.5	0.06	0.15	11	0.98	1.2

are well represented by the calculated ones and that the annealing effect due to the He irradiation during the RBS measurement must not be left out of consideration. More or less similarly good fittings are obtained also for the other implantation series (not shown).

3. Results for the undisturbed $\Delta\chi_{min}^{sim}$ versus n_{dpa}

The results of the fitting of all experimental data are given in Table II (fitting parameters) and in Fig. 7 which shows the corresponding undisturbed curves $\Delta\chi_{min}^{sim}$ versus the number of displacements per atom, n_{dpa}.

For *c* orientation no intermediate plateau, corresponding to the recombination of point defects, is observed in the experimental data. Therefore, the recombination parameter was set to $R_{pd}=0$. The critical density above which point defects are altered into clusters was taken from the value at which the slope of the experimental curves changes [see Fig. 5(a) and Table II]. The undisturbed curves obtained with these settings are given in Figs. 7(a) and 7(b) for double- and half-logarithmic plots, respectively. For all ion species, it can be seen that within the experimental error there is a good agreement of the undisturbed curves for different implantation series and for the different ion species. The latter means that there is no chemical effect of the implanted ion species and the damage formation is determined by the nuclear energy deposition.

For the *a*- and *r*-oriented samples the behavior is different than that for the *c*-oriented ones. At first, the data points of the series *S*1, starting at very low ion fluences, were fitted. Usually, these data points reach well into the fluence range of cluster formation. Though there is no recombination plateau visible in the experimental curves, a value of $R_{pd}>0$ is needed to model the data points. The value of n_{pd}^{crit} was determined as described for *c* orientation (see above). With these assumptions the data points of the series *S*1 could be well fitted yielding the parameters P_{pd}, R_{pd}, F_c, and G_c. However, it is not possible to fit the series *S*2 for the *a* and *r* orientations with the same set of parameters obtained from the corresponding series *S*1. A good fit of the calculated curves to the experimental data for the series *S*2 is only possible when either R_{pd} is enlarged or F_c is reduced. This means that the He measurement does not only cause a reduction of the defect concentration but also changes the mechanisms of damage accumulation. Within the depth range of interest, the He ions mainly lose their energy by electronic excitation or ionization of target atoms. This may result in changes of the charge state of the defects which can influence their mobility. We therefore prefer the assumption that the He measurement leads to an enhanced point defect recombination, corresponding to higher R_{pd} values in the fitting procedure. However, it should be pointed out that a similarly good fit is obtained when leaving R_{pd} constant and decreasing F_c.

The consequence of the necessary change of one of the parameters is that for *a*- and *r*-oriented samples the undisturbed curves $\Delta\chi_{min}^{sim}$ vs n_{dpa} (for short called damage-accumulation curves) are different for the different series of the same implanted ion [see Figs. 7(c)–7(f)].

When a rather high ion fluence is implanted in the first step (as done for series *S*2), the damage-accumulation curves

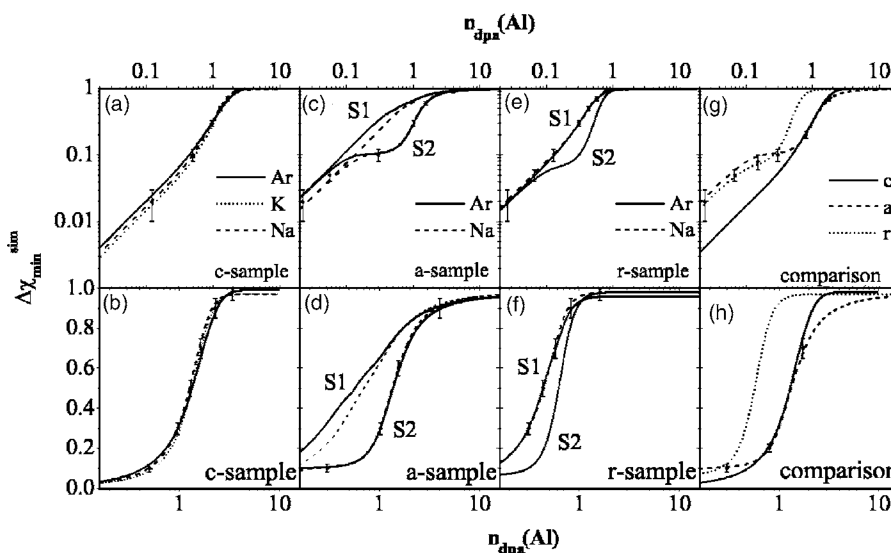

FIG. 7. The undisturbed fluence dependence, represented by $\Delta\chi_{min}^{sim}$, for *c*-oriented [(a) and (b)], *a*-oriented [(c) and (d)], and *r*-oriented [(e) and (f)] samples plotted vs n_{dpa}(Al). For better visibility all graphs are given in double-[(a), (c), and (e)] and in half-logarithmic scale [(b), (d), and (f)]. The experimental error is indicated by arbitrary data points and *S*0, *S*1, and *S*2 denote measurement series on different samples. A comparison of the crystal orientations is given in (g) and (h), again for double- and half-logarithmic plots, respectively.

Downloaded 31 Aug 2007 to 134.30.24.17. Redistribution subject to AIP license or copyright, see http://jap.aip.org/jap/copyright.jsp

exhibit a clear intermediate plateau in the range of low fluences, where no measurements were performed. This plateau can be attributed to the balance between point defect production and recombination, both occurring due to the effect of the implanted ions. On the contrary, the situation is different when implanting many small ion fluences and performing RBS measurements after each of these implantation steps (as done in series *S*1). In this case the parameter for point defect recombination needed to fit the experimental data is much smaller. This means that the defect recombination is already realized by the analyzing He beam. Hence, it does not (or to a strongly reduced amount) manifest in the undisturbed curves that represent the effect of ion implantation alone. Thus, these damage-accumulation curves do not exhibit an intermediate plateau. This is in agreement with the results of the *c*-oriented samples in so far as there the recombination of point defects is generally not obvious and consequently, the undisturbed curves are the same for all implantation series.

For the discussion of the results, those undisturbed curves have to be used for *a* and *r* orientations that follow from the series *S*2 since they represent the damage-accumulation behavior with almost no or at least the lowest interference of the measurement. However, one must not forget that they could be obtained only in combination with the results of the formerly fitted low-fluence implantation series *S*1.

Similar to the results of the *c*-oriented samples, the influence of the implanted ion species is well represented by their energy deposition in nuclear processes and no chemical effects are detected [see Figs. 7(c) and 7(d) for *a* orientation; in the case of *r* orientation a series *S*2 exists for Ar only]. In order to compare the different crystal orientations, an ion-averaged curve for the *c* sample, a mean of the curves following from the series *S*2 for the *a* sample, and the curve corresponding to the Ar series *S*2 of the *r* sample are plotted in Figs. 7(g) and 7(h). As already mentioned above, the crystal orientation has a significant influence on the damage-accumulation behavior and the same three regions discussed for the experimental data (see above) can be distinguished for the undisturbed curves as well.

IV. DISCUSSION

A. Effects of nuclear energy loss

For all orientations the damage formation is determined by the nuclear energy deposition. A chemical effect, that is to say a significant influence of the implanted ion species, is not observed neither for the curves of damage accumulation nor for the depth profiles of defect concentration at a temperature of $T=15$ K and fluences up to $N_I=1.3\times10^{16}$ cm^{-2}.

The depth profiles of the defect concentrations obtained from the RBS data are narrower than the calculated distributions (SRIM). This is at least partly due to the dip in the defect concentration between the surface and the maximum of the distribution which may be explained by the electronic energy loss (see Sec. IV B). The surface itself seems to act as a sink since it shows an enhanced concentration of defects.

The differences in the undisturbed curves of damage accumulation, observed between the various crystal orientations, can result from two possible situations (or a superposition of both). First, the implantation is not independent of the crystal orientation. In this case the produced state of damage could be influenced by the crystal axis due to some kind of channeling effect. Second, the implantation produces the same defect structures in all orientations, but these structures have a different visibility when viewed along the various crystal axes. Then RBS analysis would detect different levels of damage though the samples are in a similar state of disorder. Estimating the critical angle for axial channeling leads to values of $\leqslant 1°$. Since all implantations took place approximately 7° off axis, this favors the second possibility. Therefore the implantation itself is assumed to be of random character with a different visibility of the defects along the different crystal axes.

From the fluence dependence of the damage accumulation at the maximum of the distribution three different regions of defect formation can be distinguished.

Region I. The low level of damage for small ion fluences indicates that in direct collisions only isolated point defects are created. If each displaced lattice atom as calculated by SRIM led to a point defect, then the efficiency for point defect production, P_{pd}, should be 1. This is indeed the case for the *a*-oriented samples and within the experimental error also for the *r*-oriented samples (see Table II). This means that the results presented in this work are consistent with the displacement energies of $E_d^{Al}=20$ eV and $E_d^{O}=50$ eV for aluminum and oxygen[3] within the experimental error. Furthermore, the results suggest that in-cascade annealing, that is to say defect recombination within the lifetime of the collision cascades of the individual ions, is low at a temperature of 15 K.

However, the efficiency for point defect production measured in *c* orientation is by a factor of 5 smaller than the expected value of 1. This can be explained by considering the different crystal structures that are seen along the various axes as shown in Fig. 8. In sapphire, the Al ions occupy $\frac{2}{3}$ of the octahedral cavities in the close-packed array made up by the O ions. The other octahedral cavities are vacant. It is somehow intuitive to assume that displaced Al ions come to rest at these vacant octahedral sites preferably. In *c* orientation the vacant cavities are hidden by normally occupied Al sites as can be seen in Fig. 8(a). Therefore, a displaced Al ion that comes to rest at one of the vacant octahedral sites is not detected by RBS channeling measurement. On the contrary, the vacant sites are visible in *a* and *r* orientations so that all displaced Al ions are indeed detected [Figs. 8(b) and 8(c)]. Thus the low value of the efficiency for point defect production in *c* orientation can be well explained by a different visibility of the defects created. The experimental results indicate that only 20% of the displaced Al ions produce random interstitials (not occupying preferred lattice sites) whereas the other 80% provide special interstitials occupying vacant octahedral sites.

A recombination of point defects due to overlapping of the collision cascades is observed for *a* and *r* orientations but not for *c* orientation. In terms of the discussion just presented, this would mean that the random interstitials do not recombine during subsequent cascades. It further suggests

Downloaded 31 Aug 2007 to 134.30.24.17. Redistribution subject to AIP license or copyright, see http://jap.aip.org/jap/copyright.jsp

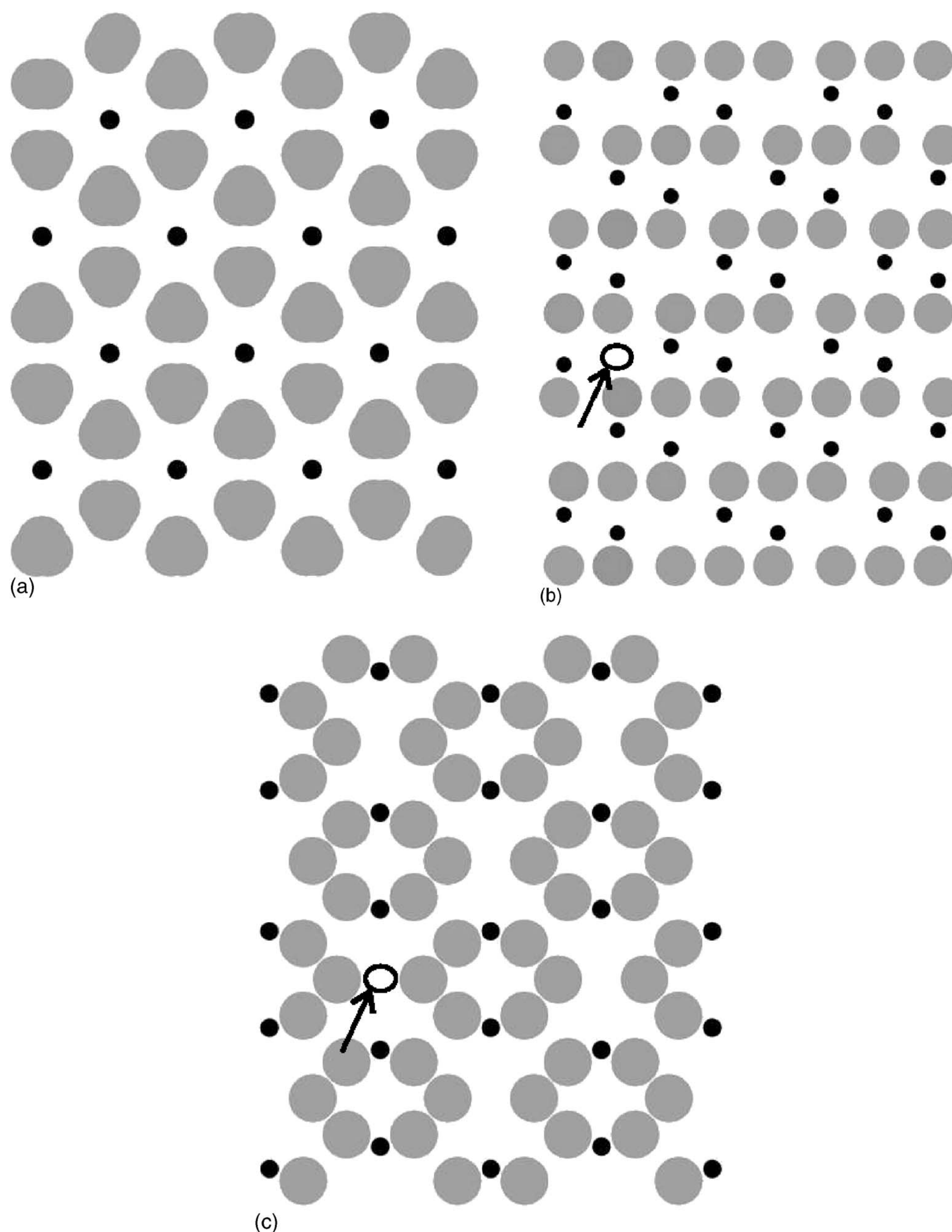

FIG. 8. Crystal structure of α-Al_2O_3 as viewed along the three different orientations *c*, *a*, and *r*. The black balls represent the aluminum ions whereas the gray balls represent the oxygen ions. The vacant octahedral sites are indicated by circles and arrows.

that displaced Al ions sitting on one of the vacant octahedral sites move to original lattice positions once the cascades start to overlap.

Region II. Above a critical concentration, the point defects are altered into clusters which show a stimulated growth with subsequent ion implantation. For *r*-oriented samples this occurs at lower n_{dpa} values than for *c*- and *a*-oriented samples. Furthermore, the curves of *a* and *r* orientations suggest some kind of saturation for the growth of the clusters that is not found for *c* orientation. Again, these differences in the behavior of the various crystal orientations could be due to a different visibility of the defect structures along the different axes. However, a discussion like the one for point defect production is not possible since the increased level of damage does not allow assumptions about the structural state of the samples. The situation becomes even more complicated due to the effect of He beam induced annealing as will be discussed in Sec. IV B.

Region III. A comparison of the behavior of the different orientations indicates that in this stage the samples are highly damaged but not yet structurally amorphous. Probably, the clusters are slowly transformed to amorphous material, yet no clear physical mechanisms can be identified from the present studies. Nevertheless, it can be concluded that the material is rendered structurally amorphous at very high n_{dpa} values ($n_{\mathrm{dpa}} > 20$ dpa) only. This is in agreement with earlier studies of McHargue and co-workers, in which the critical value for amorphization of sapphire was found to be between 55 and 90 dpa (Refs. 7, 10, and 19) at 77 K.

Downloaded 31 Aug 2007 to 134.30.24.17. Redistribution subject to AIP license or copyright, see http://jap.aip.org/jap/copyright.jsp

B. Effects of electronic energy loss

Ionizing radiation can promote the recovery of displacement damage in many ceramic insulators by enhancing the mobility of point defects (see Ref. 4 and references therein). Several different mechanisms have been proposed in order to explain this effect. The mechanism referred to as *ionization-induced diffusion* assumes that due to the electronic energy loss the charge state of a point defect is altered, leading to a significantly lower migration energy. Another explanation is based on the concept that a high concentration of electron-hole pairs may alter the bond lengths and thus the migration energy. A third proposition is that electron-hole pair recombination or deexcitation of electronic states may provide enough thermal energy to induce point defect migration.

For analyzing He ions the ratio of electronic to nuclear stopping power is about the critical value for ionization-induced diffusion reported in Ref. 4. Therefore, we attribute the He beam induced annealing during the RBS measurement to the electronic energy loss of the He ions. Annealing of defects was also found during the analysis of ion implanted sapphire with electrons at room temperature[10] and at 90 K.[20] Probably the most striking observation in connection with the annealing behavior is the huge influence of crystal orientation (see Fig. 3 in Sec. III B). As already discussed in Sec. IV A, there are several possible explanations for such an effect. One possibility is that the effect of the electronic energy loss is the same for all orientations. But since the defect structures have a different visibility along the various axes, the observed annealing is different as well. Another possibility is to assume that the incident He beam leads to an alignment or other structural changes of the defects. These structural changes would probably depend on the axis along which the He ions are incident, thus resulting in a different response of the defect structures for the different orientations. Alignment of the defect structures due to the He beam would also have consequences for the subsequent damage formation. The initial state of the sample for the next implantation step would depend on the axis of RBS measurement leading to actual differences in the defect structures for the various crystal orientations even if the implantation itself is of random nature. A third explanation is based on the concept that the implantation itself is not random, yielding different defect structures for the various axes. These may then show a different behavior under ionizing radiation.

As already mentioned in Sec. IV A, there are deviations between the experimental and calculated depth profiles of the defect concentration. It was checked that the dip near the surface observed in the DICADA profiles when compared with the SRIM distributions is not due to the RBS measurement. This rules out the electronic energy loss of the He ions as source of the enhanced recombination of defects. However, sapphire generally seems to be a material where electronic energy loss leads to damage recovery rather than damage formation. Therefore, we propose that the reduced defect concentration near the surface is caused by the electronic energy loss of the implanted ions. In this case the ratio of electronic to nuclear stopping power is certainly below the critical value. The excitation of the electronic system of the sample may nevertheless have an influence on the defects produced. This proposition is supported by the prediction of Zinkle *et al.* that ionization produced by the primary ion beam is much more effective than ionization produced by a second source.[4] However, other effects such as the surface acting as a sink for defects might contribute to a reduced defect concentration as well.

V. SUMMARY

In the present work, the damage formation and accumulation in α-Al_2O_3 of c, a, and r orientations after irradiation with Na, K, and Ar at 15 K was studied. Analysis was done by RBS channeling measurement without changing the sample temperature of 15 K.

Defect annealing was observed during the RBS measurement with 1.4 MeV He ions. It can be understood in terms of the electronic energy loss of the He ions which may cause changes in the charge state of the defects, thus enhancing their mobility. This results in actual damage recovery or in the alignment of the defect structures. The same mechanism probably occurs due to the electronic energy loss of the implanted ions, leading to a dip in the depth profiles of the defect concentration between the surface and the maximum of the distribution.

An existing model was modified to provide an analytical formula with a set of free parameters which describes the defect formation as a function of the ion fluence. Taking into account the He beam induced annealing the experimental data were fitted using this formula. From the set of parameters determined in this way the undisturbed curves of damage accumulation were obtained. The results, exhibiting the effect of the nuclear energy loss of the implanted ions, mainly show three different stages of defect formation. At very low ion fluences only isolated point defects are formed. The efficiency for that is well reproduced by SRIM calculations using displacement energies of $E_d^{Al}=20$ eV and $E_d^{O}=50$ eV for aluminum and oxygen, respectively. Only for c-oriented samples is the efficiency for point defect production found to be lower, which can be explained by a heavily reduced visibility of the created defects along this particular crystal axis. Point defect recombination is observed when the collision cascades start to overlap with increasing ion fluence. Above a critical concentration of point defects these are altered into clusters, which grow significantly during further implantation, thus forming the second stage of damage accumulation. The third stage is formed by a kind of saturation of the clusters and the gradual transformation to amorphous material. Structural amorphization is assumed to occur only after the implantation of high ion fluences corresponding to a number of displacements per atom larger than 20 dpa. No influence of the chemical properties of the implanted ion species was observed.

[1] C. W. White, C. J. McHargue, P. S. Sklad, L. A. Boatner, and G. C. Farlow, Mater. Sci. Rep. **4**, 41 (1989).
[2] C. J. McHargue, Mater. Sci. Eng., A **253**, 94 (1998).
[3] S. J. Zinkle and C. Kinoshita, J. Nucl. Mater. **251**, 200 (1997).
[4] S. J. Zinkle, V. A. Skuratov, and D. T. Hoelzer, Nucl. Instrum. Methods Phys. Res. B **191**, 758 (2002).
[5] C. J. McHargue, P. S. Sklad, and C. W. White, Nucl. Instrum. Methods

Downloaded 31 Aug 2007 to 134.30.24.17. Redistribution subject to AIP license or copyright, see http://jap.aip.org/jap/copyright.jsp

Phys. Res. B **46**, 79 (1990).
[6]E. D. Specht, D. A. Walko, and S. J. Zinkle, Nucl. Instrum. Methods Phys. Res. B **84**, 323 (1994).
[7]C. J. McHargue, G. C. Farlow, G. M. Begun, J. M. Williams, C. W. White, B. R. Appleton, P. S. Sklad, and P. Angelini, Nucl. Instrum. Methods Phys. Res. B **16**, 212 (1986).
[8]E. Alves, M. F. da Silva, J. G. Marques, J. C. Soares, and K. Freitag, Nucl. Instrum. Methods Phys. Res. B **141**, 353 (1998).
[9]H. Naramoto, Y. Aoki, and H. Abe, Nucl. Instrum. Methods Phys. Res. B **127/128**, 599 (1997).
[10]G. C. Farlow, P. S. Sklad, C. W. White. C. J. McHargue, and B. R. Appleton, Mater. Res. Soc. Symp. Proc. **60**, 387 (1986).
[11]C. J. McHargue, E. Alves, M. F. da Silva, and J. C. Soares, Nucl. Instrum. Methods Phys. Res. B **148**, 730 (1999).
[12]E. Alves, M. F. da Silva, J. C. Soares, T. Monteiro, J. Soares, and L. Santos, Nucl. Instrum. Methods Phys. Res. B **166**, 183 (2000).
[13]B. Breeger, E. Wendler, W. Trippensee, Ch. Schubert, and W. Wesch, Nucl. Instrum. Methods Phys. Res. B **174**, 199 (2001).
[14]K. Gärtner, Nucl. Instrum. Methods Phys. Res. B **227**, 522 (2005).
[15]J. F. Ziegler, J. P. Biersack, and U. Littmark, *The Stopping and Range of Ions in Solids* (Pergamon, New York, 2003).
[16]C. S. Schnohr, E. Wendler, K. Gärtner, K. Ellmer, and W. Wesch, Nucl. Instrum. Methods Phys. Res. B (in press).
[17]C. S. Schnohr, Diploma thesis (English), Friedrich-Schiller-Universität Jena, 2005.
[18]N. Hecking, K. F. Heidemann, and E. TeKaat, Nucl. Instrum. Methods Phys. Res. B **15**, 760 (1986).
[19]C. W. White, G. C. Farlow, C. J. McHargue, P. S. Sklad, M. P. Angelini, and B. R. Appleton, Nucl. Instrum. Methods Phys. Res. B **7/8**, 473 (1985).
[20]H. Abe, S. Yamamoto, and H. Naramoto, Nucl. Instrum. Methods Phys. Res. B **127/128**, 170 (1997).

Downloaded 31 Aug 2007 to 134.30.24.17. Redistribution subject to AIP license or copyright, see http://jap.aip.org/jap/copyright.jsp